

Retrieval of cloud pressure and oceanic chlorophyll content using Raman scattering in GOME ultraviolet spectra

Joanna Joiner,¹ Alexander P. Vasilkov,² David E. Flittner,^{3,4} James F. Gleason,¹ and Pawan K. Bhartia¹

Received 17 April 2003; revised 9 September 2003; accepted 30 September 2003; published 14 January 2004.

[1] Reliable cloud pressure estimates are needed for accurate retrieval of ozone and other trace gases using satellite-borne hyperspectral backscatter ultraviolet (buv) instruments. The cloud pressures should be consistent with the assumptions made in the retrieval algorithms. Cloud pressure can be derived from buv instruments using the properties of rotational-Raman scattering (RRS) and absorption by O₂-O₂. Here we estimate cloud pressure using the concept of a Lambert-equivalent reflectivity (LER) surface that is also used in many trace gas retrieval algorithms. An LER cloud pressure (P_{LER}) algorithm is being developed for the ozone monitoring instrument (OMI) that will fly on NASA EOS Aura. As a demonstration, we apply the approach to data from the global ozone monitoring experiment (GOME) in the 355–400 nm spectral range. GOME has full spectral coverage in this range at relatively high spectral resolution with a very high signal-to-noise ratio. This allows for more accurate estimates of cloud pressure than were possible with its predecessors SBUV and TOMS. We also demonstrate for the first time the retrieval of oceanic chlorophyll content using oceanic Raman scattering in buv observations. We compare our retrieved P_{LER} with cloud top pressures, P_{top} , derived from the infrared ATSR-2 instrument on the same satellite for overcast situations. The findings confirm results from previous studies that showed retrieved P_{LER} from buv observations is systematically higher than IR-derived P_{top} . Simulations using Mie-scattering radiative transfer algorithms with O₂-O₂ absorption show that these differences can be explained by increased absorption within and below the cloud as well as between multiple cloud decks.

INDEX TERMS: 0320 Atmospheric Composition and Structure: Cloud physics and chemistry; 0399 Atmospheric Composition and Structure: General or miscellaneous; 0669 Electromagnetics: Scattering and diffraction; 3360 Meteorology and Atmospheric Dynamics: Remote sensing; **KEYWORDS:** cloud, Raman, radiative transfer

Citation: Joiner, J., A. P. Vasilkov, D. E. Flittner, J. F. Gleason, and P. K. Bhartia (2004), Retrieval of cloud pressure and oceanic chlorophyll content using Raman scattering in GOME ultraviolet spectra, *J. Geophys. Res.*, 109, D01109, doi:10.1029/2003JD003698.

1. Introduction

[2] Accurate cloud pressures are needed for a variety of remote sensing problems including trace gas retrievals. Thermal infrared satellite data have traditionally been used to estimate cloud-top pressure (P_{top}) for cloud climatological data sets [e.g., Rossow and Schiffer, 1991]. Methods based on absorption in the O₂ A band [e.g., Koelemeijer *et al.*, 2001] and rotational-Raman scattering (RRS) [Joiner

and Bhartia, 1995] (JB95) have also been developed to estimate cloud pressure from satellite-borne instruments.

[3] JB95 derived Lambert-equivalent reflectivity (LER) cloud pressures (P_{LER}) using RRS with the Nimbus-7 total ozone mapping spectrometer (TOMS) and solar backscatter ultraviolet (SBUV) radiometer continuous spectral scan observations. RRS contributes to the filling-in and depletion of solar Fraunhofer lines in Earth backscattered spectra at ultraviolet wavelengths [e.g., Kattawar *et al.*, 1981; Joiner *et al.*, 1995; Chance and Spurr, 1997]. This filling-in is known as the Ring effect [Grainger and Ring, 1962] and its inclusion in satellite retrievals of trace gases is important [e.g., Vountas *et al.*, 1998].

[4] JB95 derived reasonable P_{LER} with TOMS and SBUV despite several limitations including the relatively low signal-to-noise ratio of TOMS and large pixel size (200 km²) of SBUV. P_{LER} from TOMS and SBUV was systematically greater than P_{top} from the coincident

¹NASA Goddard Space Flight Center, Laboratory for Atmospheres, Greenbelt, Maryland, USA.

²Science Systems and Applications Inc., Lanham, Maryland, USA.

³Institute of Atmospheric Physics, University of Arizona, Tucson, Arizona, USA.

⁴Also at NASA Langley Research Center, Hampton, Virginia, USA.

Nimbus-7 temperature-humidity infrared radiometer (THIR). This difference was explained by the fact that P_{LER} retrieved using UV observations is an effective pressure that would be observed if the cloud and atmosphere below it is replaced with a Lambertian surface. Scattering within and beneath the cloud effectively increases the retrieved P_{LER} to a value greater than that of P_{top} .

[5] Enhanced RRS in a cloudy atmosphere was simulated in a radiative transfer model (SCIATRAN) with Mie scattering [e.g., *de Beek et al.*, 2001 and references therein]. They compared their model results with satellite data from the global ozone monitoring experiment (GOME) and ground-based measurements at wavelengths between 390 and 400 nm where filling-in of the solar Fraunhofer Ca lines occurs. Their results showed good agreement between model and measurements where local conditions could be estimated with reasonable accuracy. In the nadir-viewing GOME geometry, their model showed that the filling-in depends on cloud optical thickness (τ) when $\tau < \sim 50$. At $\tau > 50$, the filling-in reaches an asymptotic limit and the dependence on P_{top} is similar to that of P_{LER} shown in JB95.

[6] Understanding Raman and Rayleigh scattering in a cloudy atmosphere is important for the interpretation of data from instruments such as TOMS, SBUV, and GOME. These instruments are a primary data source used to produce global climatologies and estimate trends of ozone and other trace gases [e.g., *Stolarski et al.*, 1992; *Gleason et al.*, 1993; *McPeters et al.*, 1996; *Burrows et al.*, 1999]. Errors in the assumed cloud pressure can produce non-negligible errors in retrieved total column ozone [*Koelemeijer and Stammes*, 1999] from buv instruments. It has also been shown that using infrared-derived cloud top pressures produces errors in retrieved total column ozone if clouds are treated as Lambertian due to unaccounted for ozone absorption within clouds [*Newchurch et al.*, 2002; *Liu et al.*, 2003]. The use of P_{LER} may therefore be more appropriate than IR-derived P_{top} in trace gas retrieval algorithms that use the LER assumption.

[7] Cloud pressures are also needed to study long term and seasonal variations in tropical tropospheric ozone derived from cloud slicing techniques [e.g., *Chandra et al.*, 1998, 1999; *Ziemke and Chandra*, 1999]. *Ziemke et al.* [1998] derived total tropospheric column ozone (TCO) without a direct cloud measurement in the tropics by assuming that deep convective clouds reach the tropopause. *Ziemke et al.* [2001] combined TCO from this method with upper tropospheric ozone derived from cloud slicing using cloud pressures from the Nimbus 7 THIR to estimate the lower tropospheric ozone. If a direct and appropriate cloud pressure was available, the cloud slicing technique could perhaps be applied more accurately and extended to other latitudes.

[8] There are several concepts that are used both to retrieve cloud properties and to account for cloud effects in retrieval algorithms. Without a collocated imager, there is not enough information in UV/Vis spectral measurements to independently determine sub-pixel cloud fraction and cloud pressure without making additional assumptions. Some of the common methods that have been used are (1) The LER approach: P_{LER} is used with an assumed cloud fraction of unity. This approach was used in the early TOMS total

ozone retrieval versions with a cloud climatology [*McPeters et al.*, 1993]. (2) A mixed LER approach (MLER): The LER assumption is combined with the independent pixel approximation (IPA) given by

$$I^{\text{obs}} = (1 - f)I^{\text{clear}} + fI^{\text{cloud}} \quad (1)$$

where I^{obs} is the observed radiance, f is the cloud fraction, and I^{clear} and I^{cloud} are the clear-scene and cloudy-scene radiances. The cloud fraction can be estimated using assumed values of clear (surface) and cloudy reflectivities, R^{clear} and R^{cloud} , respectively. This method is used in recent TOMS algorithms with an IR-based cloud pressure climatology [see, e.g., *Hsu et al.*, 1997]. (3) The previous two approaches can be used with a Mie scattering cloud model in place of the LER model. More assumptions about cloud properties (such as cloud geometrical thickness and droplet size distributions) must be made with this approach. The estimate of cloud fraction could be derived independently e.g., with a sub-pixel counting approach from a collocated imager (e.g., <http://cfa-www.harvard.edu/tkurosu>).

[9] In this paper we use approach 2, the MLER method, to develop an algorithm targeted for the ozone monitoring instrument (OMI) that will fly on NASA's earth observing system (EOS) Aura satellite [*Stammes et al.*, 1999]. The algorithm is designed to be used in conjunction with some of the trace gas retrievals being developed for OMI that also use the MLER approach.

[10] We demonstrate the concept using data from GOME. We will focus exclusively on situations where a pixel is likely to be completely cloud covered to facilitate a more straightforward comparison with infrared retrievals. The approach is generalizable to situations of broken or partial cloud using the IPA as demonstrated by *Hsu et al.* [1997]. The cloud fractions and pressures derived using the typical assumptions with this approach are not necessarily realistic but effective cloud fractions/pressures that explain the observed radiances. The derived effective cloud pressure/fraction combination in this situation is not unique as it depends strongly on the assumed values of R^{clear} and R^{cloud} . However, such an approach has been found to produce reasonable estimates of total ozone under partly cloudy conditions [*Hsu et al.*, 1997].

[11] We extend the spectral range and coverage of the previous studies to retrieve cloud pressure using GOME observations between 355 and 400 nm. Within this wavelength region there are two O₂-O₂ absorption bands. RRS affects observations throughout this spectral region. Absorption from O₃ and other trace gases is very small.

[12] Oceanic Raman scattering (ORS) contributes significantly to the Ring effect [e.g., *Kattawar and Xu*, 1992; *Vasilkov et al.*, 2002 and references therein]. It has been observed in buv observations and compared with a physical model [*Vasilkov et al.*, 2002]. Chlorophyll and dissolved organic matter (DOM) absorb UV radiation in the ocean. This absorption decreases filling-in due to ORS. *Vountas et al.* [2003] have shown that neglect of ORS in the retrieval of trace gases, such as BrO and HCHO from GOME, can cause significant errors. We examine the potential of using buv observations to determine chlorophyll from the high-frequency spectral structure of earthshine spectra in clear conditions.

[13] We briefly describe the GOME and OMI instruments in section 2. The forward (radiative transfer) and inverse (retrieval) models are described in sections 3 and 4, respectively. We discuss retrieval errors and sensitivities in section 5. In section 6, we compare retrievals of P_{LER} from GOME with P_{top} from collocated along track scanning radiometer-2 (ATSR-2) observations. We compare the observational results qualitatively with theoretical simulations. We also compare GOME retrievals of chlorophyll content with those from SeaWiFS. Finally, we examine radiance residuals as a check on our forward and inverse models. Conclusions and suggestions for future work are given in section 7.

2. GOME and OMI Instruments

[14] The GOME instrument was launched aboard the European space agency's (ESA) second European remote sensing satellite (ERS-2) in 1995 [Burrows *et al.*, 1999]. The ERS-2 is in a near-polar sun-synchronous orbit with a mean equator crossing time of 10:30 LST and a mean altitude of 785 km.

[15] GOME is a double monochromator that measures the earthshine radiance and solar irradiance between 240 and 790 nm in four spectral channels. Solar irradiance measurements are made once per day. In this paper we use data from channel 2 that contains measurements in the wavelength range 312–406 nm at a spectral resolution of 0.17 nm.

[16] The nominal across-track swath width is 960 km and consists of 3 pixels that cover a ground area of 40×320 km. However, in this paper we use data in the 3 days per month small swath mode where the ground pixels are 40×80 km for a swath width of 240 km. The smaller pixel mode is more desirable for cloud studies.

[17] In comparison, OMI will have a smaller footprint (nominally 13×24 km) and a larger swath (giving near-global daily coverage rather than global coverage every 3 days for GOME). The three channels of OMI cover the wavelength range 270–500 nm. Therefore unlike GOME, OMI does not have the ability to retrieve cloud pressure in the O_2A band. The spectral resolution at the wavelengths considered here is 0.45–0.63 nm. The OMI spectrum will be more highly sampled than that of GOME.

3. Forward Model

[18] In this section, we first discuss the radiative transfer models used for the atmosphere and ocean. As these models are too slow for use in an operational algorithm, the last subsection describes how the models are incorporated into tables for a computationally efficient lookup scheme.

3.1. TOMRAD Radiative Transfer Model

[19] The normalized (by the incoming solar irradiance) backscattered intensity, I_R , observed at the top of the atmosphere can be formulated using a Lambert-equivalent reflectivity (LER) model with a Lambertian surface that can generally encompass either the ground, a cloud, or some combination of the two, and incorporate the effects of aerosol and water-leaving radiance from the ocean. The LER model can be written as

$$I_R = I_R(R = 0) + RI_g\gamma/(1 - RS_b), \quad (2)$$

where R is the Lambert-equivalent reflectivity, $I_g = F/\phi$, F is the total radiance reaching the surface, γ is the transmittance of the radiance reflected from the surface, and S_b is the fraction of the reflected surface radiance that is scattered by the atmosphere back to the surface. Both I_g and γ can be separated into direct and diffuse components.

[20] The forward model used here to compute these components at every iteration of scattering is similar to that used by Joiner *et al.* [1995] and is commonly referred to as TOMRAD. TOMRAD is the offspring (several generations removed) of work done originally by Dave [1964]. TOMRAD accounts for molecular scattering and gaseous absorption using the successive orders of scattering method.

[21] Polarization of the scattered light is modeled using a modification of the classic Rayleigh scattering phase matrix due to molecular anisotropy and Raman scattering [Ahmad and Bhartia, 1995]. The King correction factors computed by Bates [1984] are used to correct the Rayleigh (molecular) phase matrix. Although no frequency redistribution of the Raman scattered energy is explicitly computed by TOMRAD, the successive order method allows for this to be approximated as done by Joiner *et al.* [1995].

[22] Any number of absorbing gases can be included in the atmosphere and can have absorption coefficients that are quadratic with temperature. The lower reflecting surface is diffuse and follows Lambert's cosine law. While Dave's original work was done for a plane-parallel atmosphere, TOMRAD has corrections for a spherical atmosphere. These corrections compared well with results from a fully spherical model under most viewing geometries with solar zenith angles up to 88° [Caudill *et al.*, 1997].

3.2. Rotational-Raman Scattering (RRS)

[23] We compute RRS filling-in based on Joiner *et al.* [1995]. As in Joiner *et al.* [1995], we treat O_2 as a simple linear molecule [Penney *et al.*, 1974] which should be sufficient at the spectral resolution considered here [Sioris, 2001]. We extended the approach to off-nadir satellite observations. The only modification necessary is to account for the satellite zenith angle in the calculation of the scattering angle.

[24] To analyze limitations of the RRS model of Joiner *et al.* [1995] and obtain insight into its basic assumptions, the model was reexamined. The radiative transfer equation for inelastic scattering [Vountas *et al.*, 1998] was solved using the straightforward successive orders of scattering method. It appeared that a solution for the inelastic component of radiation can be expressed through the elastic component at every order of scattering only if certain assumptions are valid. One assumption is that changes to the optical depth of the atmosphere and the single scattering albedo within the RRS band (i.e., for wavelengths of RRS lines) are small. This is true for Rayleigh scattering in the spectral range under consideration because the typical width of the RRS band is about 4 nm. However, this assumption may not be valid for wavelengths where the spectral dependence of the ozone absorption is not smooth within the spectral range of 4 nm such as in the Huggins bands.

[25] In Joiner *et al.* [1995], light that is Raman scattered more than once is neglected. This amounts to a small net loss of radiation. Accounting for this radiation is computationally expensive as it involves multiple convolutions. If

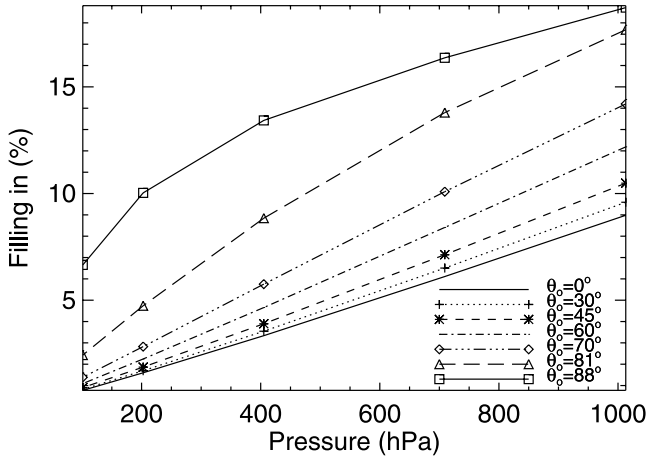


Figure 1. Filling-in at Ca K line as a function of P_{LER} at GOME spectral resolution and $R = 65\%$, satellite zenith angle $\theta = 15^\circ$, and azimuth angle $\phi = 0^\circ$.

instead, we assume that this energy is retained in the first-order-scattered Raman spectrum, we arrive at the relationship

$$\bar{k}_n = \frac{1 - \bar{f}_o^n}{1 - \bar{f}_o} \bar{k}_1, \quad (3)$$

where \bar{k}_n is the filling-in factor for the n th order and $1 - \bar{f}_o$ is the solid-angle average fraction of energy contained in Raman lines in a single scattering. The filling-in factor is defined by Joiner *et al.* [1995] as the percent difference between radiance computed with and without inelastically scattered light. The above approximation is reasonable as a significant amount of the formerly lost energy is scattered back to the same wavelengths of the single-scattered Raman spectrum. This formulation presents a small difference in total filling-in with that computed using the relationship $\bar{k}_n = n\bar{k}_1$ in Joiner *et al.* [1995].

[26] Finally, we examine the assumption that photons scattered more than once or those encountering the ground or cloud/aerosol will in subsequent scatterings be illuminated from all directions by unpolarized light [Kattawar *et al.*, 1981]. This assumption allows for an efficient calculation of the filling-in. Sioris [2001] developed a model that included polarization and phase-function effects for a limb-viewing geometry. He found that the phase function approaches isotropy at about three orders of scattering. For his geometry and an unpolarized observation, his model produced only a small difference (about 2%) with the approximate model of Kattawar *et al.* [1981]. However, for polarized measurements, these effects are non-negligible. We computed an upper-limit for our nadir-viewing unpolarized measurement by assuming the maximum phase-function error at every order of scattering above one for which photons did not encounter the ground. The upper limit on the error is approximately 5% for high reflectivities indicative of cloud and increases to about 13% for low reflectivities typical of clear scenes. We will account for the error in our retrieval algorithm through the estimated forward model error that is part of the observation error.

[27] Figure 1 shows the dependence of the Ca K line (~ 393 nm) filling-in on P_{LER} at GOME spectral resolution. The RRS dependence on pressure is nearly linear for solar zenith angles $\theta_o < 80^\circ$.

[28] The reflectivity (R) dependence of the filling-in (or $\text{O}_2\text{-O}_2$ absorption) is important because it primarily determines how sensitive the retrieved P_{LER} will be to an error in absolute calibration as will be discussed below. One way to verify a cloud pressure retrieval is to retrieve the land surface pressure over varying terrain in clear conditions. Therefore understanding the R dependence is important at both high and low values of R .

[29] Figure 2 shows the R dependence of filling-in. The sharp decrease in RRS with increasing R at low θ_o and low values of R is related to an increase in the reflected component of the radiance that does not undergo Rayleigh/Raman scattering. However, the filling-in begins to increase with R at about $R = 0.4$, where an increase in the scattered light between the surface and atmosphere, related to the S_b term in (2), becomes important.

3.3. $\text{O}_2\text{-O}_2$ Absorption in the Ultraviolet

[30] There are two relatively weak absorption bands of $\text{O}_2\text{-O}_2$ in the 350–400 nm wavelength range (360.4 nm and 380.2 nm). In addition, there is a stronger band near 477 nm that is observed by GOME and will also be observed with OMI. A separate cloud pressure retrieval algorithm is being developed for OMI based on this $\text{O}_2\text{-O}_2$ absorption band [Acarreta and de Haan, 2002].

[31] The $\text{O}_2\text{-O}_2$ absorption cross sections are taken from Greenblatt *et al.* [1990]. To characterize the effect of $\text{O}_2\text{-O}_2$ absorption at the band center, we use a concept similar to the filling-in factor. We define δ as the fractional change in normalized radiance due to $\text{O}_2\text{-O}_2$ absorption. Because $\text{O}_2\text{-O}_2$ absorption decreases the normalized radiance, δ is negative.

[32] Figure 3 shows the simulated spectral dependence of δ at different values of P_{LER} . The wiggles in the line center at low pressure are due to weak O_3 absorption.

[33] Figure 4 is similar to Figure 1 but for $\text{O}_2\text{-O}_2$ absorption rather than RRS. Because of the pressure-

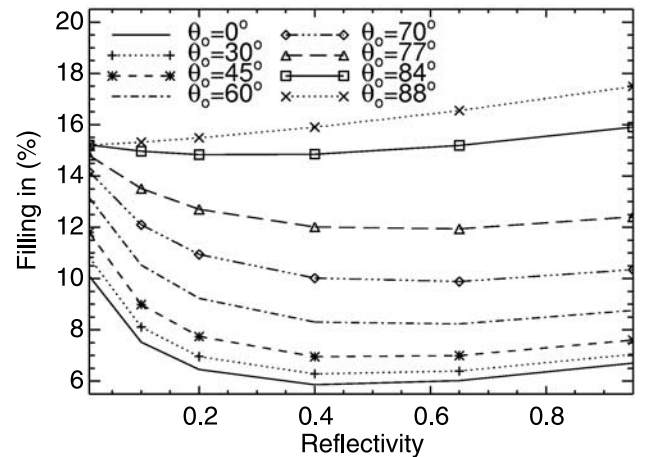


Figure 2. Similar to Figure 1 but with R as the abscissa, computed for $P_{\text{LER}} = 700$ hPa, $\theta = 15^\circ$, and $\phi = 0^\circ$.

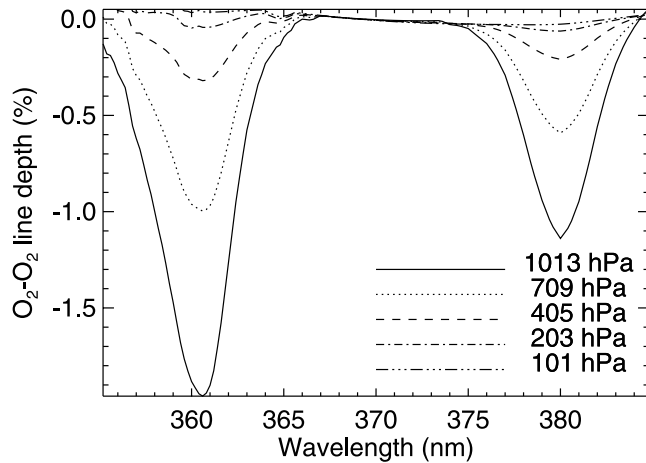


Figure 3. Fractional change in simulated radiance due to O_2-O_2 absorption computed with $R = 65\%$, $\theta_o = 60^\circ$, $\theta = 15^\circ$, and $\phi = 0^\circ$.

squared dependence of the absorption, these curves are less linear than those for RRS. The sensitivity to P_{LER} is relatively low compared with RRS at lower pressures.

[34] Figure 5 shows the R dependence of O_2-O_2 absorption which is qualitatively different than that of RRS. The increase in R at low R increases O_2-O_2 absorption due to the increased pathlength between the reflecting surface and atmosphere by decreasing the $1-RS_b$ term in the denominator of the second term in equation (2). In contrast, the filling-in due to RRS decreases with increasing R at low R owing to a decrease in the fractional amount of observed Rayleigh scattering.

3.4. Oceanic Raman Scattering (ORS) in the Ocean

[35] A radiative transfer model for ocean filling-in has been developed by *Vasilkov et al.* [2002] and compared with GOME observations at the Ca K line. The model was able to simulate the observed excess filling-in in clear waters and decreased filling-in over turbid waters using climatological values of chlorophyll content.

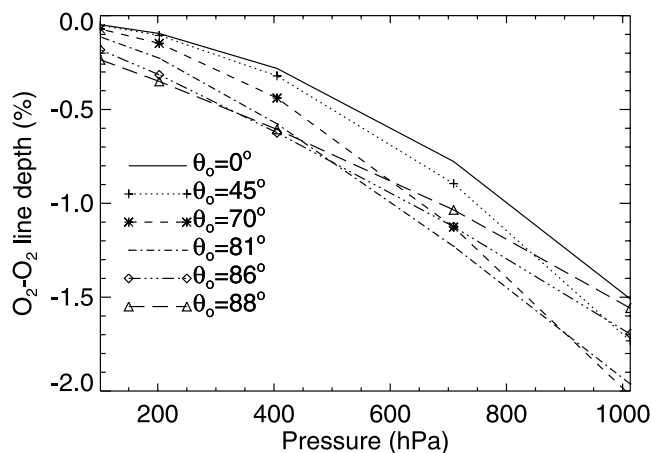


Figure 4. O_2-O_2 line depth at 360 nm as a function of P_{LER} computed at $R = 65\%$, $\theta = 15^\circ$, and $\phi = 0^\circ$.

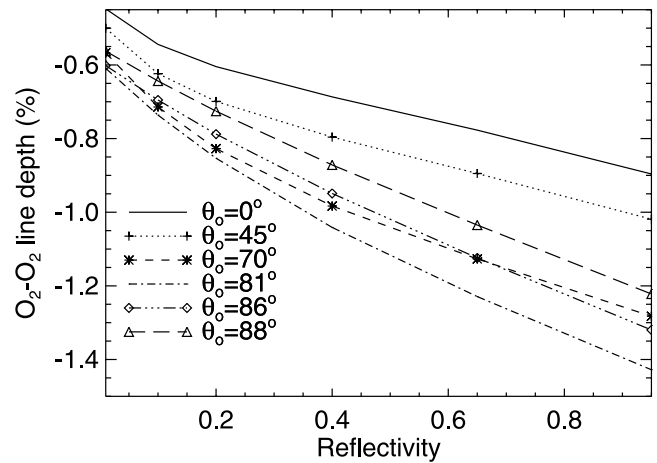


Figure 5. Similar to Figure 2 (same viewing geometry) but for O_2-O_2 absorption at 360 nm.

[36] There remains significant uncertainty in the pure water absorption at these wavelengths [e.g., *Vasilkov et al.*, 2002]. However, the results of *Vasilkov et al.* [2002] supported the lower values measured in a laboratory by *Quickenden and Irvin* [1980] and *Pope and Fry* [1997] and we use their results here.

[37] Figure 6 shows the spectral dependence of the filling-in, calculated at GOME resolution, due to both atmospheric and oceanic Raman scattering. For shorter wavelengths, the ocean filling-in is negative representing a net depletion of energy due to the dominance of energy transfer from those wavelengths to longer wavelengths over the energy gain from shorter wavelengths. The spectral signature is similar for atmospheric and oceanic filling-in. However, the magnitude of the oceanic filling-in decreases with decreasing wavelength owing to the reduced amount of radiation reaching the surface at excitation wavelengths in the ozone Huggins bands. The atmospheric filling-in at OMI resolution is reduced as compared with that shown here for GOME by slightly less than 50%. The oceanic filling-in at OMI resolution, however, has only a slightly smaller magnitude than that shown here for GOME [*Joiner et al.*, 2002]. As will be shown in subsection 6.2, it is possible to determine both chlorophyll content and P_{LER} (including aerosol effects) simultaneously from buv observations.

3.5. Table Generation

[38] Tables of the iteration values output from the TOMRAD code were generated for wavelengths between 340 and 400 nm for a single O_3 profile (because O_3 absorption is very weak in this spectral range, a single profile will suffice) for 5 different surface pressures, 10 solar zenith angles, 6 satellite zenith angles, and 7 azimuth angles. Using a GOME solar spectrum, a second set of tables of the RRS filling-in and normalized radiance for these geometries were generated at GOME spectral resolution for 6 reflectivities and 5 pressures. A table for the oceanic filling-in was created using the *Vasilkov et al.* [2002] model for the same geometries and for 7 values of chlorophyll content (0.02, 0.05, 0.1, 0.2, 0.5, 1.0, 10.0 mg/m^3), 2 reflectivities (0.05 and 0.10), and one

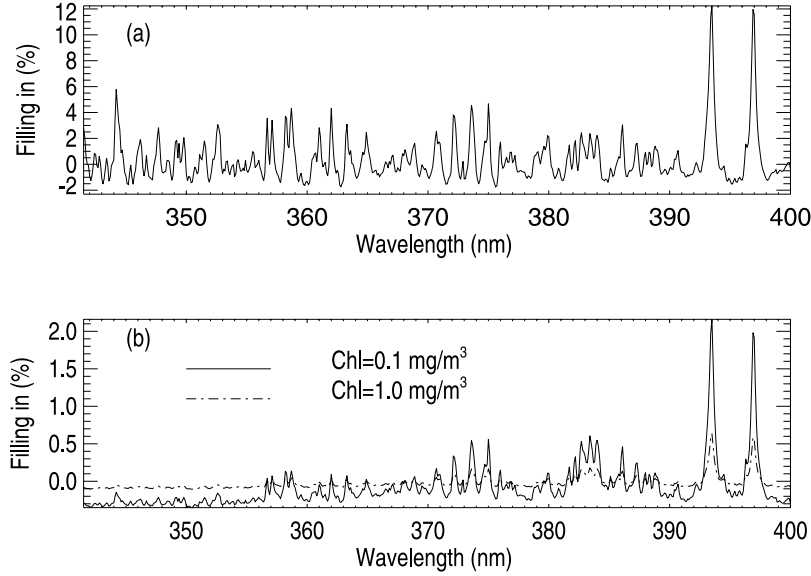


Figure 6. (a) Atmospheric Raman filling-in; (b) oceanic Raman filling-in for two chlorophyll concentrations, $R = 10\%$, $\theta_o = 45^\circ$, top-of-the-atmosphere nadir view.

pressure (1013 hPa). These tables will be used to compute radiances by linear interpolation, as described in the next section, for the retrieval of P_{LER} .

4. Inverse Model

4.1. Reflectivity Calculation

[39] The Lambert-equivalent reflectivity, R , is calculated at 373.2 nm by inversion of (2). This wavelength was chosen such that it is relatively free of RRS and $\text{O}_2\text{-O}_2$ absorption.

4.2. P_{LER} Retrieval by Least-Squares Fitting

[40] P_{LER} is retrieved by an iterative minimum-variance (least-squares) solution of the form

$$x_{n+1} = x_n + \left(H^T(W)^{-1}H \right)^{-1} H^T(W)^{-1}(y_{\text{obs}} - y_{\text{calc}}), \quad (4)$$

where x_n is the state vector estimate at iteration n , H is the Jacobian matrix (partial derivatives of the observation vector with respect to the state vector) and the superscript T denotes transpose, W is the observation error covariance which includes measurement and forward model errors, and y_{obs} and y_{calc} are vectors of observed and calculated radiances, respectively. The retrieval error covariance, E , is then given by

$$E = \left(H^T(W)^{-1}H \right)^{-1}. \quad (5)$$

[41] At every iteration a quantity χ is computed, defined by

$$\chi = \left([y_{\text{resid}}] W^{-1} [y_{\text{resid}}]^T \right)^{0.5} / N, \quad (6)$$

where N is the number of observations and y_{resid} , called the radiance residual, is defined as $y_{\text{resid}} = y_{\text{obs}} - y_{\text{calc}}$. Iterations

continue until $(\chi_{n-1} - \chi_n)/\chi_{n-1} < 0.03$. The pixel is flagged if convergence does not occur within 6 iterations. The algorithm typically converges in 2–3 iterations.

[42] The observation vector includes normalized radiances in the 355–400 nm spectral range. All parameters are retrieved simultaneously using observations in this spectral range. The observations are spline-interpolated to the table wavelengths that have a 0.2 nm spacing. This greatly reduces the amount of computation required for interpolation as compared with interpolating table values to observed wavelengths.

[43] The observation error covariance, W , is a diagonal matrix with the square root of the diagonal set conservatively to 1% of the observed value. This value of 1% is significantly higher than the GOME radiometric noise which we estimate to be about 0.2% based on examinations of radiance residuals. The value of 1% is used to account for other errors such as forward modeling errors and errors due to GOME undersampling. A diagonal matrix is used both because the error correlations are unknown and difficult to estimate, and the use of a full matrix would significantly increase the computational load of the algorithm.

[44] The state vector includes three coefficients to form a quadratic fit of the low-frequency component of the radiances (i.e., $A + B\lambda + C\lambda^2$), two coefficients to correct for wavelength differences between the solar irradiance and earth-view spectra, shift ($\Delta\lambda$) and squeeze ($\hat{\lambda}$), and P_{LER} . The quadratic coefficients account for Rayleigh scattering as well as calibration errors so that the P_{LER} is determined only from the high-frequency component of the spectra. The wavelength shift parameter accounts for any wavelength differences due to unaccounted for Doppler shift. Over ocean or large lakes, chlorophyll content (CHL) can be added to the state vector.

[45] The initial values of A , B , and C are determined by a polynomial fit to the given spectrum. Values of -0.006 nm and 0.99998 were chosen for the first guess $\Delta\lambda$ and $\hat{\lambda}$, respectively, which are typical of the retrieved values for

Table 1. Errors (Standard Deviation) From Linear Estimate^a

θ_o	R , %	σ_P , hPa	$\sigma_{\Delta\lambda}$, nm	$\sigma_{\hat{\lambda}}$	σ_{CHL} , mg/m ³	CHL, mg/m ³	$r_{P, CHL}$, %
84.7	83.1	26	6.9e-4	2.8e-5	N/A	N/A	N/A
50.1	83.4	24	6.7e-4	2.7e-5	N/A	N/A	N/A
41.5	5.0	46	6.7e-4	2.7e-5	N/A	N/A	N/A
26.5	6.2	128	6.7e-4	2.7e-5	0.256	0.423	93
24.3	8.9	117	6.8e-4	2.7e-5	0.086	0.176	93
33.4	9.3	111	6.8e-4	2.7e-5	0.033	0.094	93

^aN/A indicates situation where oceanic quantities are not retrieved over land.

GOME data. P_{LER} is initialized to 500 hPa. When applicable the chlorophyll is initialized to its climatological value derived from gridded annual mean SeaWiFS data (<http://daac.gsfc.nasa.gov/data/dataset/SEAWIFS/index.html>). These initial conditions are selected to minimize the number of iterations in the algorithm. We found little sensitivity of the results to the initial guess except for CHL in high chlorophyll-content waters where information content is poor as will be discussed in the next section.

[46] The magnitudes of $\Delta\lambda$ and $\hat{\lambda}$ are assumed to be constant over the given spectral interval. Therefore the spectrally shifted and squeezed quantities are calculated as $f(\lambda + \Delta\lambda)$ and $f(\hat{\lambda})$, respectively.

[47] The radiances y_{calc} are computed by linear interpolation of the tables in R , θ_o , θ , ϕ , and P_{LER} . The P_{LER} , CHL, $\Delta\lambda$, and $\hat{\lambda}$ Jacobians are computed by finite differences. Jacobians for the other parameters are determined analytically.

[48] There are several potential sources of error with the MLER approach. The high surface reflectivities of snow and ice will produce errors. For the operational OMI algorithm, we plan to use a snow/ice mask to flag contaminated pixels. In such a situation, we will assume a cloud fraction of unity to retrieve P_{LER} . This should produce reasonable results in a total ozone algorithm. Absorbing aerosol can affect RRS and produce errors in a cloud pressure retrieval. Errors will also occur in the presence of sea glint. These conditions are relatively easy to detect and we therefore plan to flag contaminated pixels.

5. Sensitivity Analysis

5.1. Retrieval Error Estimates Due to Observational Error

[49] Using (5), we can estimate the errors in retrieved parameters. This linear error estimate is computed at the final iteration of the retrieval process. The estimate assumes that observation biases and spectrally-correlated errors are negligible. As shown in the next section, these assumptions are not met, so that this is not an absolute error estimate. These are retrieval error estimates based on observational errors (forward model error and instrument noise). We do not consider here retrieval errors due to errors in the parameters that are held fixed, such as the assumed surface albedo.

[50] The error estimate is unique for every situation, because the Jacobian depends upon the satellite geometry, reflectivity, and the number of retrieved parameters. Table 1 gives representative values of error standard deviations (σ) for P_{LER} , $\Delta\lambda$, $\hat{\lambda}$, and CHL along with the retrieved CHL, θ_o , R , and the correlation between P_{LER} and CHL errors ($r_{P, CHL}$). The values in Table 1 are calculated assuming a

Gaussian, uncorrelated observation error with $\sigma = 1\%$. The errors are given for either fully cloudy or clear pixels.

[51] Typically, for a fully cloudy pixel with high reflectivity and CHL not included in the state vector, the estimated error in P_{LER} is ~ 25 hPa. The error does not depend significantly on P_{LER} . If chlorophyll is not included in the state vector, the error correlations are all less than 10%. For clear conditions (low reflectivity), the P_{LER} errors nearly double to about 50 hPa while the correlations remain at less than 10%. The wavelength shift and squeeze errors are always low and are virtually uncorrelated with the other parameters. This is because the spectral structure induced by these parameters is nearly orthogonal to that produced by the others, including P_{LER} . The errors at OMI spectral resolution were computed using observational errors of 0.5% and were found to be roughly half of those shown here for GOME with the more conservative estimate of 1% for observational errors [Joiner et al., 2002].

[52] When CHL is added to the state vector under clear conditions along with P_{LER} , the P_{LER} error doubles approximately to about 120 hPa. This is because an extra degree of freedom (CHL) has been added to the state vector and its sensitivity is not completely orthogonal to that of P_{LER} . The P_{LER} error is highly correlated with the CHL error (93%). Therefore a positive error in P_{LER} will correspond to a positive error in CHL and will be of similar magnitude in terms of the fractional standard deviation.

[53] In practice, we plan to report CHL only in cloud-free conditions. However, we will fit the CHL spectral feature in cases of partial cloud to aid the P_{LER} retrieval. Aerosol is expected to have a similar effect to clouds on filling-in. Therefore the CHL errors given here would be appropriate for aerosol-loaded conditions. However, if the data are screened for aerosol contamination and the surface pressure is assumed to be known and P_{LER} is removed from the state vector eliminating one degree of freedom, the CHL errors will be smaller than those shown here. This is analogous to the example of smaller P_{LER} errors over land when CHL is not included in the state vector.

[54] In overcast conditions, the chlorophyll signal should be very small owing to a reduction in the amount of light reaching the ocean surface as well as a reduction in amount of light reaching the satellite that has penetrated the ocean surface. Therefore errors in P_{LER} will be essentially the same as those reported above when chlorophyll is not included in the state vector. The broken cloud scenario may require the simultaneous retrieval of CHL and P_{LER} and thus will produce the larger errors in P_{LER} as given in Table 1. However, ozone retrievals will have less sensitivity to cloud pressure errors in this case and so larger errors are tolerable.

[55] The CHL error depends upon the retrieved value of CHL. The error is higher, both in absolute amount and percentage, for higher values of chlorophyll. This is because the sensitivity begins to drop off at higher values of CHL where the contribution of oceanic Raman scattering becomes negligible [see Vasilkov et al., 2002]. In these samples, CHL errors range from approximately 60% at CHL = 0.42 to about 35% at CHL = 0.094.

5.2. Sensitivity to Absolute Calibration Error

[56] Because P_{LER} and CHL are determined from the high-frequency spectral structure of RRS and O₂-O₂

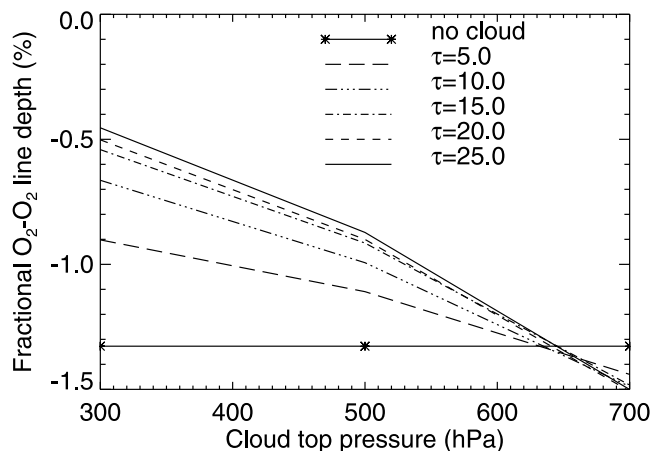


Figure 7. $\text{O}_2\text{-O}_2$ (360 nm) absorption dependence on cloud-top pressure and τ , $\theta_0 = 45^\circ$, $\theta = 0^\circ$, $\phi = 0^\circ$.

absorption, errors in absolute calibration contribute only through the determination of R . Filling-in due to RRS varies strongly with R at low R and weakly with R at high R . Therefore in overcast conditions, the retrieval of P_{LER} will be relatively insensitive to absolute calibration.

[57] For example, at high values of R , a 10% error in absolute calibration (Earth radiance with respect to solar flux) will produce a change of about 10% in R . The resulting change in P_{LER} is only about 20–30 hPa. However, at low R , a 10% calibration error may change R by only about 3%, but this will produce a change in P_{LER} of about 100 hPa. The accuracy of the GOME absolute calibration is not precisely known. However, the applied polarization correction could yield a significant error (up to 10%) in the operational calibration in the UV [Schutgens and Stammes, 2003].

5.3. Mie Scattering Simulations

[58] To investigate the expected differences between P_{LER} and P_{top} , we use a full Mie-scattering radiative transfer model in a cloudy atmosphere in the $\text{O}_2\text{-O}_2$ bands. The calculations were performed using the University of Arizona Gauss-Seidel iteration code [Herman and Browning, 1965]. Clouds were assumed to be horizontally and vertically uniform. A C1 cloud model with a modified gamma size-distribution of water droplets was used [Deirmendjian, 1969]. Simulations were carried out for three cloud scenarios with physical cloud-top pressures of $P_{\text{top}} = 300, 500$, and 700 hPa. Geometrical thickness of the clouds was defined by a constant pressure difference of 200 hPa between the top and bottom cloud pressures. The simulations included aerosol scattering. A maritime aerosol model [Shettle and Fenn, 1979] with a relative humidity of 70% was assumed with the aerosol optical thickness of 0.15 at 550 nm. The surface reflectivity for all calculations was 5%. RRS was not included in the calculations.

[59] Figure 7 shows $\text{O}_2\text{-O}_2$ absorption line depth versus the physical cloud top pressure for clouds with different values of τ at 360 nm. The $\text{O}_2\text{-O}_2$ absorption dependence on τ converges at about $\tau = 25$. Figure 7 illustrates the increase in $\text{O}_2\text{-O}_2$ absorption with decreasing τ . For example, a $\tau =$

5.0 cloud at 300 hPa gives the same amount of $\text{O}_2\text{-O}_2$ absorption as a $\tau = 20$ cloud at 500 hPa.

[60] An interesting effect is the response for the lowest cloud. It can be seen that there is enhanced absorption for the thick cloud as compared with the thin cloud or no cloud. This is the result of the reflectivity dependence of $\text{O}_2\text{-O}_2$ absorption that increases the photon path length between the cloud and scattering atmosphere above.

[61] To give some idea of how the enhanced absorption will affect a P_{LER} retrieval, Figure 8 shows derived values of P_{LER} for different cloud conditions, where P_{LER} is derived using $\text{O}_2\text{-O}_2$ absorption at 360 nm only (no Raman scattering). Note that results will be slightly different if RRS is included. The derived P_{LER} uses the reflectivity that would be retrieved for a given cloud assuming a homogeneous cloud covered the entire pixel. P_{LER} and P_{top} can differ by as much as about 175 hPa. The differences are larger for the higher clouds. For photons that penetrate through the clouds, there is more opportunity for Rayleigh scattering beneath the high clouds than the low clouds. Therefore more photons will be backscattered back through the cloud and observed from above for the higher clouds in this example with low surface reflectivity.

6. Results and Comparisons With Other Data

[62] Our objective in this section is to examine the differences between P_{top} and P_{LER} to see whether they agree with expected differences.

6.1. Cloud Pressure Comparison With ATSR-2

[63] The retrieved P_{LER} can be compared with P_{top} derived from thermal infrared observations from the along track scanning radiometer-2 (ATSR-2). ATSR-2 also flies on ERS-2 and produces visible and infrared images of the Earth in 7 channels at a spatial resolution of 1 km [Mutlow et al., 2000]. A data set of ATSR-2 P_{top} and cloud fraction has been produced where ATSR-2 pixels are collocated with the GOME small pixels and averaged over the same ground footprint [Watts et al., 1998].

[64] In this comparison, we chose $R^{\text{clear}} = 15\%$. Although most surface reflectivities are less than 15%, this value has

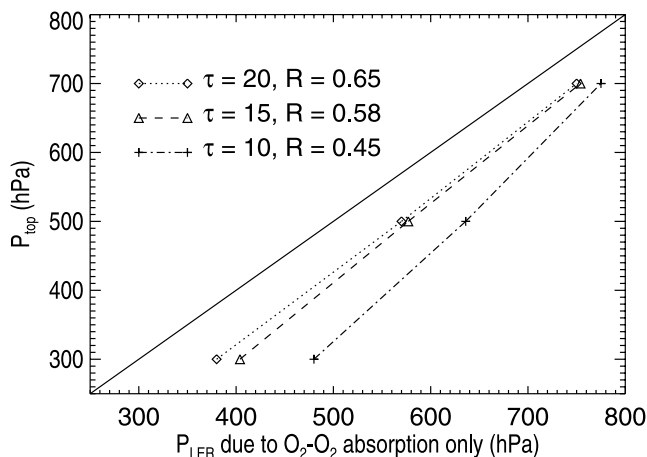


Figure 8. Derived P_{LER} using $\text{O}_2\text{-O}_2$ (360 nm) absorption (no RRS) versus physical cloud top (P_{top}) for geometry of Figure 7.

Table 2. Statistics for Selected Individual GOME Orbits and Differences Between GOME P_{LER} and ATSR P_{top} as Explained in Text

Orbit	No. Pixels Total	No. Match ATSR	No. Match Overcast	No. $R < .15$	No. $0.15 < R < .40$	Mean, hPa	σ , hPa	r
80324124	1417	473	157	267	384	169	70	0.91
80324142	1416	474	124	438	345	191	105	0.76
80324156	1416	474	149	346	392	183	101	0.58
80324156 ^a	1416	474	73	346	392	146	61	0.82
80324174	1415	474	163	416	303	208	106	0.77
80324192	1415	472	129	280	482	238	90	0.85
all	7079	2367	722	1747	1906	197	98	0.80

^aLatitudes above 50°N excluded.

produced good results in ozone algorithms as it partially accounts for aerosol effects. Some cloud contamination will occur in pixels with $R < 15\%$. Typically, the value of R^{cloud} that is used in trace gas retrievals is 80%.

[65] Our comparisons with ATSR-2 derived cloud fractions showed that a significant number of overcast pixels had reflectivities as low as 40%. Although we plan to use a value of 80% in the operational OMI algorithm, here we assume $R^{\text{cloud}} = 40\%$ and provide a cloud comparison only for pixels where $R^{\text{cloud}} > 40\%$ and the retrieved ATSR-2 cloud fraction is 90–100% thus indicating cloud covering a majority of the pixel. This provides a good sample for our comparisons of P_{LER} with ATSR-2-derived P_{top} under a variety of different conditions. Clouds with lower (higher) reflectivities correspond to lower (higher) optical thickness. For assumed clear ($R < 15\%$) and overcast ($R > 40\%$) pixels, all calculations are performed at the retrieved value of R .

[66] Broken clouds may be present for scenes with reflectivities above 40%. Mixed scenes ($0 < f < 1$) will not be considered here as they are problematic for inter-comparison studies. However, the method should produce an effective cloud fraction/pressure combination that is consistent with observed radiances and appropriate for use in trace gas retrievals in a mixed scene.

[67] We examine five orbits from 24 March 1998. The cloudy pixels used here occurred over all types of terrain (land, ocean, and ice). Table 2 gives statistics for the GOME P_{LER} and ATSR P_{top} comparison (mean difference (mean), standard deviation of the difference (σ), and correlation coefficient r) for five orbits separately and all orbits combined along with the numbers of clear pixels, those matched up with ATSR-2, and those used for the cloudy statistics as described above. Although there is some variability among the different orbits, the overall results are similar. P_{LER} from GOME is consistently higher than P_{top} from ATSR-2 and the correlation between the two is relatively high.

[68] The correlation and standard deviation are better than was obtained by JB95 with TOMS/SBUV THIR for $R > 40\%$, most likely due to the higher signal-to-noise ratio of GOME. The bias is of the same sign, however slightly larger than JB95. The correlation for orbit 80324156 (0.58) is significantly lower than that from the other orbits. A significant number of cloudy pixels in this orbit were over Greenland and extreme northern Canada. The reflectivities of these pixels were very high (above 0.90) indicating ice/snow under cloud. The correlation for these pixels was low. When latitudes above 50°N are excluded, the correlation is similar to the other orbits (0.82).

[69] Significantly higher cloud pressures derived from the GOME O_2A band as compared with ATSR-2 were also

reported by Koelemeijer and Stammes [2000]. They used a similar MLER approach where cloud fractions were derived along with cloud pressures. The GOME/ATSR-2 differences were most pronounced where the derived cloud fractions were close to one.

[70] Figure 9 shows the ground path of GOME orbit 80324174 that we will examine in more detail. This orbit has a good sample of cloud free pixels over ocean where chlorophyll content varies from very high values near the North American coast to very low in the Pacific desert. There are overcast conditions at high latitudes in both hemispheres and also near the equator.

[71] Figure 10 is a scatter diagram of P_{LER} obtained using GOME versus P_{top} from collocated ATSR-2. Figure 11 shows that there is a high correlation between IR P_{top} and UV P_{LER} and that the differences are more systematic than random. For example, the pixels between 65 and 70°S have a significantly smaller difference than those between 65 and 70°N. These systematic differences are much greater than the expected error due to random noise. With the exception of a few pixels between 55 and 60°N, P_{LER} is always greater than P_{top} as expected. Note that no clear pixels are used in these figures, only those for which the ATSR cloud fraction is greater than 90%.

[72] The $P_{\text{LER}}-P_{\text{top}}$ correlation is high for the equatorial region where high, optically thick clouds are observed. The correlations are also relatively high for the geographical region between 40 and 60°S. Most clouds in the region have moderate optical depths. The differences are larger for the northern region between 40 and 75°N. Most clouds in this region are optically thick.

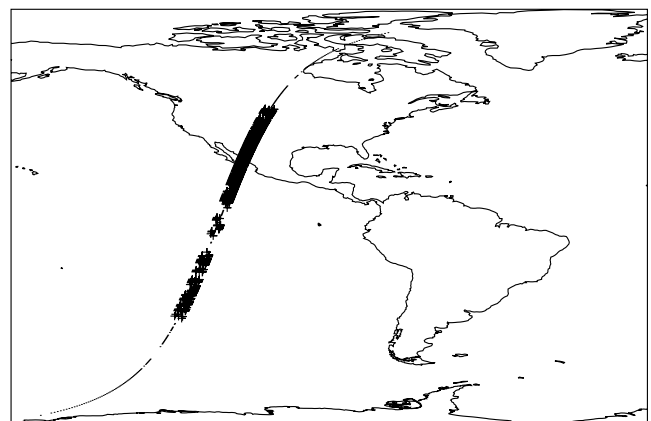


Figure 9. GOME orbit 80324174; Dots, $R > 40\%$ and collocated with ATSR, +: $R < 15\%$.

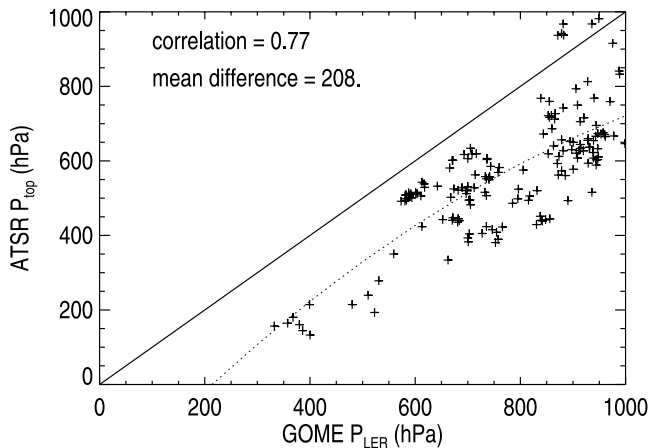


Figure 10. Scatter diagram of retrieved cloud pressures for orbit 80324174. Dotted line is second order polynomial fit.

[73] There was no obvious dependence of the $P_{\text{LER}}-P_{\text{top}}$ difference on R (as might be expected based on Figure 8) or θ_o . There is also no obvious dependence on the surface type (non-ice/snow covered land versus ocean) indicating a significant sensitivity to ORS in the pixels examined here. This leaves open the possibility that the differences may be related to other cloud geometrical parameters such as the physical thickness. Simulations with the Mie scattering $\text{O}_2\text{-O}_2$ model have shown that increasing the cloud vertical extent, while keeping all other cloud parameters fixed (for clouds with $\tau > 5$), increases the $\text{O}_2\text{-O}_2$ absorption. This in turn increases the retrieved P_{LER} .

[74] However, the observed $P_{\text{LER}}-P_{\text{top}}$ differences are sometimes significantly larger than those expected from a single cloud layer as shown approximately in Figure 8. Multiple cloud decks or clouds over snow/ice may explain these large differences. Comparisons of infrared-derived P_{top} with conventional ground-based reports indicate that multiple clouds decks may be present as much as 50% of the time on spatial scales similar to those considered here [Menzel et al., 1992].

[75] In order to simulate the effects of multiple cloud layers or clouds above ice/snow, we computed $\text{O}_2\text{-O}_2$

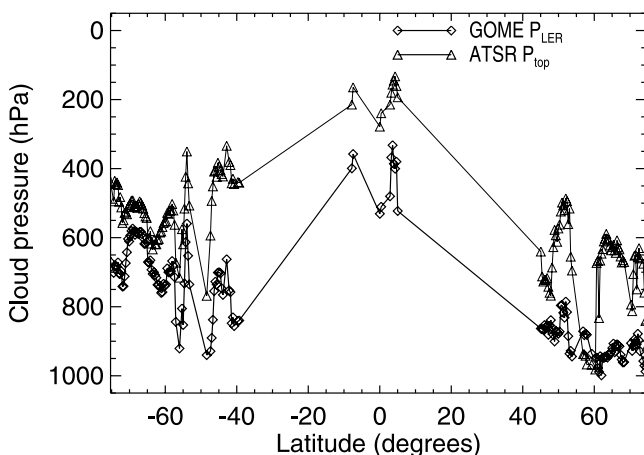


Figure 11. Comparison of retrieved cloud pressures.

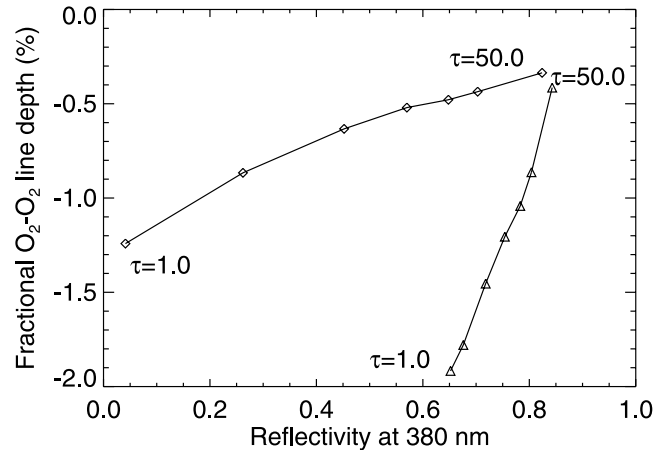


Figure 12. $\text{O}_2\text{-O}_2$ absorption at 360 nm computed using the Mie scattering model at $\theta_o = 45^\circ$, $\theta = 0^\circ$, and $\phi = 0^\circ$ as described in the text for $\tau = 1, 5, 10, 15, 20, 25$, and 50. Triangles, pseudo two-layer cloud; diamonds, single layer cloud.

absorption at 360 nm using the Mie scattering code with a cloud top at 600 hPa (100 hPa geometrical thickness) above a highly reflecting surface ($R = 65\%$) at 912 hPa that represents a lower-altitude cloud. The calculations were performed for several values of optical thickness between 1 and 50. The $\text{O}_2\text{-O}_2$ absorption is compared with that from a simulated single layer cloud (same geometry) above a 1013 hPa low-reflectivity surface ($R = 5\%$) in Figure 12. As $\tau \rightarrow 0$, $R \rightarrow R^{\text{surface}}$ (where R^{surface} is the R of the lower cloud or ice/snow surface) as expected. As τ increases, the absorption from the pseudo-two-layer model approaches that of the single-layer.

[76] In the pseudo-two-layer model with $\tau < 50$ for the upper cloud, the $\text{O}_2\text{-O}_2$ absorption is greater than that for the single layer model with an equivalent 380 nm reflectivity (this is a standard TOMS wavelength used for reflectivity). Since the upper cloud of the two-layer model is semi-transparent, some of the absorption that occurs within and below the upper cloud, but above the bottom cloud, can be seen from above. In the single cloud layer case, most of the radiation that penetrates the cloud does not get scattered or reflected upward from below due to the low surface reflectivity and thus does not return through the cloud to be observed from above.

6.2. Retrieval of Chlorophyll and Comparison With SeaWiFS

[77] In order to evaluate the ocean Raman model as well as the cloud pressure retrieval algorithm, we performed retrievals over cloud-free ($R < 15\%$) pixels. Several methods were tested to retrieve the scene pressure over ocean: (1) No ocean Raman scattering is included in the radiative transfer calculations. (2) Ocean Raman scattering is included using climatological values of chlorophyll concentrations. (3) Chlorophyll is treated as an additional state variable within the retrieval algorithm.

[78] Figure 13 shows retrieved P_{LER} over clear ocean scenes for GOME orbit 80324174 where the expected value is ~ 1000 hPa. Not accounting for ocean Raman scattering leads to significant errors in the retrieved P_{LER} . The use of

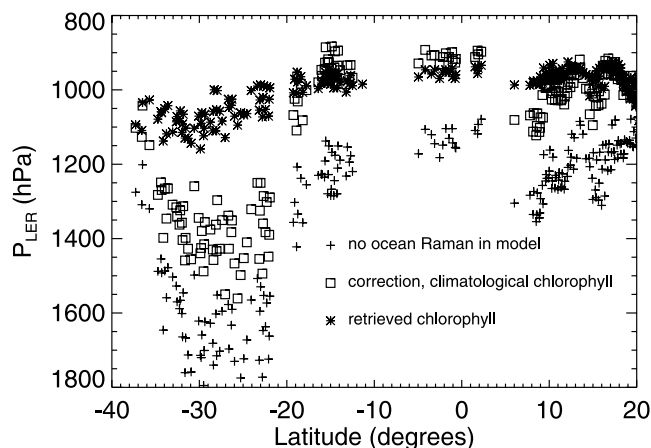


Figure 13. Retrieved P_{LER} over clear ocean using different methods described in text.

climatological chlorophyll reduces but does not eliminate errors in the retrieved P_{LER} . The remaining error could result from the actual chlorophyll deviating from the climatological values used here or errors in the ocean radiative transfer model including the UV optical parameters.

[79] Allowing chlorophyll to be an additional state variable in the algorithm significantly improves the retrieval of surface pressure. The best agreement is between 20°S and 20°N where the ocean model has been optimized. We assumed a single value for total ozone (225 Dobson units) appropriate for low latitudes in the generation of the ORS tables. The spectral dependence of the filling-in due to ORS should vary with total ozone for wavelengths shorter than about 370 nm. The computed filling-in for the ocean component will be overestimated for total ozone amounts greater than 225 DU owing to overestimated radiance at the ocean surface for the shorter excitation wavelengths. This may lead to errors in how the retrieved P_{LER} and CHL are partitioned.

[80] Figure 14 shows the retrieved chlorophyll concentration and for comparison, the annual mean climatological values that were used as a first guess, and weekly data from the Sea-viewing Wide Field-of-view Sensor (SeaWiFS)

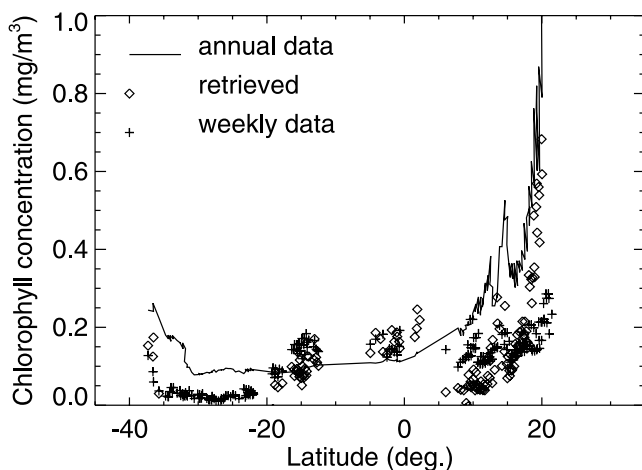


Figure 14. Retrieved chlorophyll and annual-mean and weekly values from SeaWiFS.

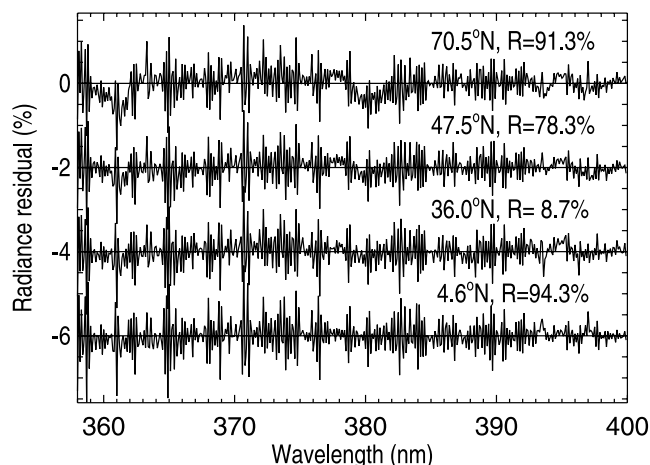


Figure 15. Radiance residual spectra from four different GOME pixels, offset by 0, -2, -4, -6% for clarity. The latitude and reflectivity are given above.

[Hooker *et al.*, 1992]. Similar spatial variations in chlorophyll are retrieved using ORS including very low values in the southern Pacific and higher values approaching the North American coast. Note that there is decreasing sensitivity to chlorophyll at larger chlorophyll amounts for our retrievals. The retrieved chlorophyll values at the higher levels remain close to the first guess and the associated error bars are larger.

[81] There is some indication that, as expected from the results in Table 1, P_{LER} and CHL errors are correlated. For example, at latitudes near -15° and between 5 and 15°, the retrieved P_{LER} is lower than the expected 1013 hPa. At these latitudes CHL is also generally lower than the weekly SeaWiFS data.

[82] This initial comparison is very promising considering the relatively large GOME footprint, uncertainties in water optical properties, and simplified treatment of the ozone dependence. The results further support the lower values of water absorbance measured by Quickenden and Irvin [1980] and Pope and Fry [1997]. The higher values measured by Smith and Baker [1981] produced negative chlorophyll values in the relatively clear waters of the Pacific desert region.

6.3. Radiance Residuals

[83] Figure 15 shows y_{resid} at convergence for several different GOME pixels. Residuals are generally in the range $\pm 0.5\%$ and are comparable to those shown for lower spectral resolution instruments in Joiner *et al.* [1995]. The residuals are similar in all pixels shown which cover a wide range of conditions. Some residual features, that are reproduced in every spectrum, have also been observed in GOME trace gas retrievals [e.g., Chance, 1998]. They have been attributed, in large part, to the spectral undersampling of the GOME instrument. Thus the forward model and/or observation errors are correlated between different wavelengths. The uncorrelated component (standard deviations) is low ($\sim 0.2\%$), indicating that the GOME detector noise is extremely low at these wavelengths.

[84] For the high latitude cloudy case (high R) where the solar zenith angle is high, residuals are higher in the vicinity

of the O_2-O_2 bands. There may be an error in the O_2-O_2 cross sections, in our RRS forward model, the LER approximation, or in the observations (e.g., polarization sensitivity). Note that we did not convolve the O_2-O_2 cross sections with the GOME slit function and this may produce a small error at GOME/OMI spectral resolution. Because more wavelengths are affected by RRS and the RRS signal is larger, the algorithm fits mainly the RRS structure of the spectrum and hence the residuals are larger in the O_2-O_2 absorption bands.

[85] The residuals in the O_2-O_2 bands are smaller in the mid-latitude cloudy spectrum. One reason for this may be that the solar zenith angle is smaller. If there is an error in the O_2-O_2 cross sections, the residuals would decrease with photon pathlength or solar zenith angle.

[86] Residuals are slightly smaller in the clear pixel. The low reflectivity decreases absorption due to O_2-O_2 and would therefore decrease the residual due to a cross section error.

[87] For the high equatorial cloud, residuals in the O_2-O_2 band are relatively small. In this case, O_2-O_2 absorption is generally smaller due to the high cloud.

[88] There are several potential sources of bias including polarization effects. GOME is known to have polarization sensitivity. The operational polarization correction is applied to the spectra used here [see, e.g., *Schutgens and Stammes*, 2003] but that correction is a relatively smooth function of wavelength. It therefore does not account for higher frequency errors at Fraunhofer lines due to the fully depolarized nature of RRS described in *Kattawar et al.* [1981] and observed by *Solomon et al.* [1987].

[89] There are also indications that in some GOME spectra a single shift and squeeze combination (as opposed to spectrally-dependent shift and squeeze) is not adequate to describe wavelength differences between Earth and solar observations. We note that these spectra with higher residuals occur systematically near the same latitudes in every orbit we examined. This may be linked to temperature changes on the satellite due to solar heating and/or other instruments being turned on/off. The residuals tend to increase at high southern latitudes. Since the orbits occur at different longitudes, we do not believe that the large residuals we see in every orbit are related to the south Atlantic anomaly (SAA). However, instruments such as GOME and OMI may have systematic radiance errors in the vicinity of the SAA. We have not examined this effect for GOME, but will screen OMI data near the SAA if significant errors are found.

7. Conclusions and Future Work

[90] We have shown that P_{LER} can be retrieved using buv measurements throughout the spectral range between 355 and 400 nm. Comparisons with coincident IR-derived P_{top} show that UV-derived P_{LER} is systematically higher. Mie scattering calculations indicate that light penetrating clouds causing enhanced absorption by O_2-O_2 should indeed result in P_{LER} being higher than P_{top} . In addition, excess absorption and scattering from multiple-layer clouds significantly increases P_{LER} .

[91] We also showed that the retrieved P_{LER} over clear ocean improves when chlorophyll content is added to the

state vector. Initial comparison of retrieved chlorophyll with that derived from SeaWiFS shows that oceanic Raman scattering is a promising new technique for deriving information about chlorophyll and other UV-absorbing matter in water. The approach has high sensitivity in relatively clear waters (low chlorophyll levels) and a relatively small sensitivity to errors in absolute calibration and other atmospheric effects/constituents such as Rayleigh scattering and aerosol. We plan to investigate the sensitivity of retrieved chlorophyll and possibly dissolved organic matter to optical parameters and other aspects of the ocean radiative transfer model as well as total column ozone and cloud properties in the future.

[92] This paper focuses on a demonstration of the cloud pressure retrieval algorithm for overcast pixels. These are the situations of maximum impact on total O_3 retrievals and of the most interest for retrieving tropospheric O_3 using a cloud-slicing type of approach. We plan to extend this work to partially cloudy cases. However, additional complications will arise when intercomparing data sets from different instruments due to differences in the pixel size and thus the implied cloud fraction, especially in the presence of thin partial cloud.

[93] EOS-Aura will fly in formation with several other satellites carrying instruments designed to measure cloud properties including the VIS/IR imager moderate resolution imaging spectroradiometer (MODIS) on EOS-Aqua, a dual wavelength lidar and infrared imager on cloud-aerosol lidar and infrared pathfinder satellite observations (CALIPSO), and a 94 GHz radar on CloudSat. These instruments will make measurements over the same area within 20 minutes of OMI. We plan to examine the information content of a multi-spectral approach using passive UV, VIS, and IR observations for retrieving information about cloud vertical extent and the existence of multiple cloud decks. It is hoped that the active sensors in this satellite formation can be used to evaluate the multi-spectral concept.

[94] **Acknowledgments.** This work was supported in part by NASA under the algorithm development program for the Earth Observing System Aura Ozone Monitoring Instrument (EOS Aura OMI). The authors thank the European Space Agency (ESA), the UK Natural Environment Research Council, and the Rutherford Appleton Laboratory for their support in supplying ATSR-2 data and ESA for providing the GOME level 1 data. We also thank the SeaWiFS project (Code 970.2) and the Goddard Earth Sciences Data and Information Services Center/Distributed Active Archive Center (Code 902) at the Goddard Space Flight Center, Greenbelt, MD 20771, for the production and distribution of SeaWiFS data. We thank J. Burkholder for providing O_2-O_2 cross-section and J. Herman, P. Stammes, J. de Haan, and J. Acarreta for helpful comments. Finally, we thank several anonymous reviewers for comments that helped to improve this manuscript.

References

- Acarreta, J. R., and J. F. de Haan (2002), Cloud pressure algorithm based on O_2-O_2 absorption, *OMI Algorithm Theoretical Basis Document (ATBD-OMI-03)*, vol. 3, chap. 2, edited by P. Stammes, Greenbelt, Md.
- Ahmad, Z., and P. K. Bhartia (1995), Effect of molecular anisotropy on the backscattered UV radiance, *Appl. Opt.*, **34**, 8309–8314.
- Bates, D. R. (1984), Rayleigh scattering by air, *Planet. Space Sci.*, **32**, 785–790.
- Burrows, J. P., et al. (1999), The Global Ozone Monitoring Experiment (GOME): Mission concept and first scientific results, *J. Atmos. Sci.*, **56**, 151–171.
- Caudill, T. R., D. E. Flittner, B. M. Herman, O. Torres, and R. D. McPeters (1997), Evaluation of the pseudo-spherical approximation for backscattered ultraviolet radiances and ozone retrieval, *J. Geophys. Res.*, **102**, 3881–3890.

- Chance, K. V. (1998), Analysis of BrO measurements from the global ozone monitoring experiment, *Geophys. Res. Lett.*, **25**, 3335–3338.
- Chance, K. V., and R. D. Spurr (1997), Ring effect studies: Rayleigh scattering, including molecular parameters for rotational Raman scattering, and the Fraunhofer spectrum, *Appl. Opt.*, **36**, 5224–5230.
- Chandra, S., J. R. Ziemke, W. Min, and W. G. Read (1998), Effects of 1997–1998 El Niño on tropospheric ozone and water vapor, *Geophys. Res. Lett.*, **25**, 3867–3870.
- Chandra, S., J. R. Ziemke, and R. W. Stewart (1999), An 11-year solar cycle in tropospheric ozone from TOMS measurements, *Geophys. Res. Lett.*, **26**, 185–188.
- Dave, J. V. (1964), Meaning of successive iteration of the auxiliary equation in the theory of radiative transfer, *Astrophys. J.*, **140**, 1292–1303.
- de Beek, R., M. Vountas, V. V. Rozanov, A. Richter, and J. P. Burrows (2001), The Ring effect in the cloudy atmosphere, *Geophys. Res. Lett.*, **28**, 721–724.
- Deirmendjian, D. (1969), *Electromagnetic Scattering on Spherical Polydispersions*, 290 pp., Elsevier Sci., New York.
- Gleason, J. F., et al. (1993), Record low global ozone in 1992, *Science*, **260**, 523–526.
- Grainger, J. F., and J. Ring (1962), Anomalous Fraunhofer line profiles, *Nature*, **193**, 762.
- Greenblatt, G. D., J. J. Orlando, J. B. Burkholder, and A. R. Ravishankara (1990), Absorption measurements of oxygen between 330 and 1140 nm, *J. Geophys. Res.*, **95**, 18,577–18,582.
- Hooker, S. B., W. E. Esais, G. C. Feldman, W. W. Gregg, and C. R. McClain (1992), *An Overview of SeaWiFS and Ocean Color, SeaWiFS Technical Report Series*, vol. 1, NASA Goddard Space Flight Center, Greenbelt, Md.
- Hsu, N. C., R. D. McPeters, C. J. Seftor, and A. M. Thompson (1997), Effect of an improved cloud climatology on the total ozone mapping spectrometer total ozone retrieval, *J. Geophys. Res.*, **102**, 4247–4255.
- Joiner, J., and P. K. Bhartia (1995), The determination of cloud pressures from rotational-Raman scattering in satellite backscatter ultraviolet measurements, *J. Geophys. Res.*, **100**, 23,019–23,026.
- Joiner, J., P. K. Bhartia, R. P. Cebula, E. Hilsenrath, and R. D. McPeters (1995), Rotational-Raman scattering (Ring effect) in satellite backscatter ultraviolet measurements, *Appl. Opt.*, **34**, 4513–4525.
- Joiner, J., A. Vasilkov, D. E. Flittner, E. Bucsela, and J. F. Gleason (2002), Retrieval of cloud pressure from rotational Raman scattering, *OMI Algorithm Theoretical Basis Document (ATBD-OMI-03)*, vol. 3, chap. 3, edited by P. Stammes, Greenbelt, Md.
- Kattawar, G. W., and X. Xu (1992), Filling in of Fraunhofer lines in the ocean by Raman scattering, *Appl. Opt.*, **31**, 6491–6500.
- Kattawar, G. W., A. T. Young, and T. J. Humphreys (1981), Inelastic scattering in planetary atmospheres: I. The Ring effect, without aerosols, *Astrophys. J.*, **243**, 1049–1057.
- Koelemeijer, R. B. A., and P. Stammes (1999), Effects of clouds on ozone column retrieval from GOME UV measurements, *J. Geophys. Res.*, **104**, 8281–8294.
- Koelemeijer, R. B. A., and P. Stammes (2000), Comparison of cloud retrievals from GOME and ATSR-2, *Earth Obs. Quart.*, **65**, 25–27.
- Koelemeijer, R. B. A., P. Stammes, J. W. Hovenier, and J. F. de Haan (2001), A fast method for retrieval of cloud parameters using oxygen A band measurements from the Global Ozone Monitoring Experiment, *J. Geophys. Res.*, **106**, 3475–3490.
- Liu, X., M. J. Newchurch, and J. H. Kim (2003), Occurrence of ozone anomalies over cloudy areas in TOMS version-7 level-2 data, *Atmos. Chem. Phys. Discuss.*, **3**, 187–223.
- McPeters, R. D., et al. (1993), Nimbus-7 total ozone mapping spectrometer (TOMS) data products user's guide, *NASA Ref. Publ.*, **1323**.
- McPeters, R. D., S. M. Hollandsworth, L. E. Flynn, J. R. Herman, and C. J. Seftor (1996), Long-term ozone trends derived from the 16-year combined Nimbus 7 Meteor 3 TOMS Version 7 record, *Geophys. Res. Lett.*, **23**, 3699–3702.
- Menzel, W. P., D. P. Wylie, and K. I. Strabala (1992), Seasonal and diurnal changes in cirrus clouds as seen in four years of observations with the VAS, *J. Appl. Meteorol.*, **31**, 370–385.
- Mutlow, C. T., D. L. Smith, and M. J. Murray (2000), The Along Track Scanning Radiometer (ATSR) instruments on ERS-1 and -2, *Earth Obs. Quart.*, **65**, 1–5.
- Newchurch, M. J., X. Liu, J. H. Kim, and P. K. Bhartia (2002), On the accuracy of Total Ozone Mapping Spectrometer retrievals over tropical cloudy regions, *J. Geophys. Res.*, **106**, 32,315–32,326.
- Penney, C. M., R. L. St. Peters, and M. Lapp (1974), Absolute rotational Raman cross sections for N₂, O₂, and CO₂, *J. Opt. Soc. Am.*, **64**, 712–716.
- Pope, R. M., and E. S. Fry (1997), Absorption spectrum (380–700 nm) of pure water, II. Integrating cavity measurements, *Appl. Opt.*, **36**, 8710–8723.
- Quickenden, T. I., and J. A. Irvin (1980), The ultraviolet absorption spectrum of liquid water, *J. Chem. Phys.*, **72**, 4416–4428.
- Rossow, W. B., and R. A. Schiffer (1991), ISCCP cloud data products, *Bull. Am. Meteorol. Soc.*, **72**, 2–20.
- Schutgens, N. A. J., and P. Stammes (2003), A novel approach to the polarization correction of spaceborne spectrometers, *J. Geophys. Res.*, **108**(D7), 4229, doi:10.1029/2002JD002736.
- Shettle, E. P., and R. W. Fenn (1979), Models of the aerosols of the lower atmosphere and the effects of humidity variations on their optical properties, *TR-79-0214*, Air Force Geophys. Lab., Hanscom, Mass.
- Sioris, C. E. (2001), Filling in of absorption lines in sky spectra due to rotational Raman scattering, 133 pp., Ph.D. thesis, York University, Canada.
- Smith, R. C., and K. C. Baker (1981), Optical properties of the clearest natural waters, *Appl. Opt.*, **20**, 177–186.
- Solomon, S., A. L. Schmeltekopf, and R. W. Sanders (1987), On the interpretation of zenith sky absorption measurements, *J. Geophys. Res.*, **92**, 8311–8319.
- Stammes, P., P. Levelt, J. de Vries, H. Visser, B. Kruizinga, C. Smorenburg, G. Leppelmeier, and E. Hilsenrath (1999), Scientific requirements and optical design of the Ozone Monitoring Instrument on EOS-CHEM, *Proc. SPIE Conf. Earth Obs. Sys. IV*, **3750**, 221–232.
- Stolarski, R., R. Bojkov, L. Bishop, C. Zerefos, J. Stachelin, and J. Zawodny (1992), Measured trends in stratospheric ozone, *Science*, **256**, 342–349.
- Vasilkov, A., J. Joiner, J. F. Gleason, and P. K. Bhartia (2002), Ocean Raman scattering in satellite backscatter ultraviolet measurements, *Geophys. Res. Lett.*, **29**, 1837–1840.
- Vountas, M., V. V. Rozanov, and J. P. Burrows (1998), Ring effect: Impact of rotational Raman scattering on radiative transfer in Earth's atmosphere, *J. Quant. Spectrosc. Radiat. Transfer*, **60**, 943–961.
- Vountas, M., A. Richter, R. Wittrock, and J. P. Burrows (2003), Inelastic scattering in ocean water and its impact on trace gas retrievals from satellite data, *Atmos. Chem. Phys. Discuss.*, **3**, 2931–2962.
- Watts, P. D., C. T. Mutlow, A. J. Baran, and A. M. Zavody (1998), Study on cloud properties derived from Meteosat Second Generation Observations, *ITT no. 97/181*, 344 pp., EUMETSAT, Darmstadt, Germany. (Available at www.eumetsat.de)
- Ziemke, J. R., and S. Chandra (1999), Seasonal and interannual variabilities in tropical tropospheric ozone, *J. Geophys. Res.*, **104**, 21,425–21,442.
- Ziemke, J. R., S. Chandra, and P. K. Bhartia (1998), Two new methods for deriving tropospheric column ozone from TOMS measurements: Assimilated UARS MLS/HALOE and convective-cloud differential techniques, *J. Geophys. Res.*, **103**, 22,115–22,127.
- Ziemke, J. R., S. Chandra, and P. K. Bhartia (2001), “Cloud slicing”: A new technique to derive upper tropospheric ozone from satellite measurements, *J. Geophys. Res.*, **106**, 9853–9867.

P. K. Bhartia and J. F. Gleason, NASA Goddard Space Flight Center, Code 916, Greenbelt, MD 20771, USA. (bhartia@carioa.gsfc.nasa.gov; gleason@redwind.gsfc.nasa.gov)

D. E. Flittner, Cooperative Center for Atmospheric Science and Technology (CCAST), University of Arizona, Tucson, AZ 85721, USA. (d.e.flittner@larc.nasa.gov)

J. Joiner, NASA Goddard Space Flight Center, Code 910.3, Greenbelt, MD 20771, USA. (joiner@dao.gsfc.nasa.gov)

A. P. Vasilkov, Science Systems and Applications Inc., 10210 Greenbelt, Rd., Ste 400, Lanham, MD 20706, USA. (alexander_vasilkov@sesda.com)